Applied Catalysis B: Environmental 168-169 (2015) 274–282

Contents lists available at ScienceDirect

Applied Catalysis B: Environmental

journal homepage: www.elsevier.com/locate/apcatb

3DOM $BiVO_4$ supported silver bromide and noble metals: High-performance photocatalysts for the visible-light-driven degradation of 4-chlorophenol

Kemeng Ji[a,b], Hongxing Dai[a,*], Jiguang Deng[a], Hongjun Zang[c], Hamidreza Arandiyan[d], Shaohua Xie[a], Huanggen Yang[a]

[a] Key Laboratory of Beijing on Regional Air Pollution Control, Beijing Key Laboratory of Green Catalysis and Separation, Key Laboratory of Advanced Functional Materials, Education Ministry of China, and Laboratory of Catalysis Chemistry and Nanoscience, Department of Chemistry and Chemical Engineering, College of Environmental and Energy Engineering, Beijing University of Technology, Beijing 100124, China
[b] WPI Advanced Institute for Materials Research (AIMR), Tohoku University, Sendai 980-8577, Japan
[c] School of Environmental and Chemical Engineering, Tianjin Polytechnic University, Tianjin 300387, China
[d] Particles and Catalysis Research Group, School of Chemical Engineering, The University of New South Wales, Sydney, NSW 2052, Australia

ARTICLE INFO

Article history:
Received 8 November 2014
Received in revised form
24 December 2014
Accepted 27 December 2014
Available online 31 December 2014

Keywords:
Three-dimensionally ordered macropore
$BiVO_4$ supported AgBr
Supported noble metals
Photocatalyst
4-Chlorophenol degradation

ABSTRACT

Three-dimensionally ordered macroporous (3DOM) photocatalysts $BiVO_4$ (denoted as 3D-BiV), AgBr/3D-BiV, and 0.17 wt% M/AgBr/3D-BiV (M=Au, Pt, and Pd) were prepared using the polymethyl methacrylate-templating, low-temperature deposition, and polyvinyl alcohol-protected reduction methods, respectively. The as-prepared $BiVO_4$ possessed a good-quality 3DOM structure and a high surface area. It is found that the AgBr and noble metals were uniformly distributed on the surface of 3D-BiV. Among the M/AgBr/3D-BiV samples, the 0.17 wt% Pd/AgBr/3D-BiV sample showed the highest photocatalytic activity for the degradation of 4-chlorophenol (4-CP) under visible light illumination (i.e., complete 4-CP degradation could be achieved within 150 min), which was associated with its good 3DOM structure, high surface oxygen adspecies concentration, easy transfer and separation of photogenerated carriers, and synergistic effect between AgBr or Pd nanoclusters and $BiVO_4$.

1. Introduction

Chlorophenols are one kind of the most noxious pollutants in soil and wastewater derived from applications of pesticides, herbicides, and wood preservatives [1]. 4-Chlorophenol (4-CP), a representative of these pollutants, is harmful to the environment and human health [2]. Traditional methods for water disinfection (e.g., chlorination and ozonation) may lead to the formation of hazardous disinfection byproducts that induce carcinogenic and mutagenic diseases [3]. A desired wastewater treatment process is supposed to degrade the toxic species completely, rather than generate some hazardous intermediates. Therefore, more effective wastewater treatment technologies are highly welcome. As one of the advanced oxidation processes via efficient utilization of solar energy, semiconductor-mediated photocatalysis has been widely regarded as a promising technique for solving environmental pollution problems and achieving industrial sustainable developments [4]. TiO_2 possesses a limited sunlight absorption range (3–4% UV region of the solar spectrum) due to its large bandgap (3.2 eV for anatase), and its photocatalytic activity is usually confined by the low quantum efficiency and high recombination rate of the photogenerated carries [2]. To address this problem, modifications on TiO_2 (e.g., Au–Ag/TiO_2 [1], polyaniline (PANI)/TiO_2 [5], and $Bi_xTi_{1-x}O_2$ [6]) have been made. Recently, developing novel visible-light-responsive photocatalysts (e.g., $ZnFe_2O_4$ [2], Fe_3O_4/CeO_2 [7], Ag–AgI/Fe_3O_4@SiO_2 [8], $BiVO_4$ [9], $MCrO_4$ (M=Sr, Ba) [10], and $Bi_2O_3/TiZrO_4$ [11]) has become a hot topic. However, when some of these photocatalysts were applied to degrade 4-CP (whose permissible limit in drinking water supply is 0.5 mg/L [1,11]), the unsatisfactory photocatalytic activities or stability limit their practical application in cleaning up of pollutants under solar light illumination (Table S1). Hence, more efficient visible-light photocatalysts are highly desired to be developed so as to satisfy the demand of future environmental and energy technologies that are driven by solar energy [8].

* Corresponding authors. Tel.: +86 10 6739 6118; fax: +86 10 6739 1983.
E-mail address: hxdai@bjut.edu.cn (H. Dai).

http://dx.doi.org/10.1016/j.apcatb.2014.12.045
0926-3373/

As a promising photosensitive material, silver halide (e.g., AgBr) was reported to show efficient photocatalytic activity and high stability under visible-light irradiation, which was regarded to be partially related to the plasmonic Ag^0 species coexisting on the surface [8]. In addition, constructing a three-component nanojunction system (e.g., CdS—Au—TiO_2 [12], AgBr—Ag—Bi_2WO_6 [13], and TiO_2 nanotube/Ag—AgBr [14]) is an efficient strategy to enhance the photocatalytic activity by promoting the separation of photoexcited electron/hole pairs. Coupled metals could further improve the charge separation efficiency and enlarge the light absorption range of a composite photocatalyst [14]. Meanwhile, significant attention has been paid on heterogeneous photocatalysts containing semiconductor and plasmonic metals (e.g., Ag, Au, Pt, and Pd nanoparticles) in harvesting and converting solar energy [15]. Recently, our group have observed photocatalytic activities of three-dimensionally ordered macroporous (3DOM) $BiVO_4$ much better than that of its bulk counterpart for the degradation of phenol and dyes under visible-light illumination [16,17]. To the best of our knowledge, there have been no reports on combining all of the above features into a single photocatalyst for the visible-light-driven degradation of 4-CP.

Taking the advantages of noble metal nanoparticles, AgBr, and 3DOM $BiVO_4$ into considerations, it is envisioned that an appropriate combination of such three components can generate a photocatalyst that would show excellent photocatalytic performance for the visible-light-driven degradation of organics. Inspired by the above motivations, the present work reports a new kind of nanohybrid photocatalysts, i.e., noble metal/AgBr/$BiVO_4$ with 3DOM architecture, multiple heterojunctions, and plasmonic nanostructure, to efficiently photocatalyze the Fenton oxidation of 4-CP in the presence of H_2O_2 under visible-light irradiation.

2. Experimental

2.1. Sample fabrication

2.1.1. Fabrication of 3DOM $BiVO_4$

The monoclinic 3DOM $BiVO_4$ photocatalyst (denoted as 3D-BiV) was fabricated by adopting the ascorbic acid-assisted polymethyl methacrylate (PMMA)-templating strategy [16]. 10 mmol of NH_4VO_3, 10 mmol of ascorbic acid, 1 mL of nitric acid aqueous solution (68 wt%), and 6 mL of deionized water were first mixed at 70 °C in a 50-mL beaker and then cooled to room temperature (RT). 3.0 g of the PMMA template was soaked in the above mixture precursor solution for 3 h. After filtration and one drying procedure in air at RT, the PMMA solid was first calcined in N_2 flow (100 mL/min) at a ramp of 1 °C/min from RT to 300 °C, kept at 300 °C for 2 h, cooled to RT, and further calcined in air flow (100 mL/min) at the same heating rate from RT to 400 °C and maintained at this temperature for 2 h. For comparison purposes, a nonporous $BiVO_4$ (denoted as $BiVO_4$-bulk) sample was also prepared using a hydrothermal method [18] after calcination at 450 °C for 4 h.

2.1.2. Fabrication of AgBr/3D-BiV

The as-prepared 3D-BiV (1.0 g), deionized water (246 mL), and KBr (0.0714 g) were added sequentially to a glass bottle (10 mL) in an ice–water isotherm bath. After bubbling in the dark for 2 h, an AgBr aqueous solution (0.01 mol/L) with 53.3 mL of polyvinyl pyrrolidone (PVP) as protecting agent (Ag/PVP monomer mass ratio = 1:1.5) was gradually dipped in the above mixture, followed by bubbling for 5 h to get a solid precursor. Subsequently, the obtained AgBr/3D-BiV sample was dried at 80 °C for 1 h, annealed at 200 °C for 2 h, washed with deionized water, and dried at 80 °C for 2 h again. The theoretical loading of AgBr was 10 wt%.

2.1.3. Fabrication of M/AgBr/3D-BiV

The M/AgBr/3D-BiV (M=Pt, Au or Pd) with trace amount of the noble metal (loading = ca. 0.2 wt%) were prepared via a bubbling-assisted sol deposition–adsorption route. The M aqueous solution (0.01 mol/L) containing noble metal cations was first prepared using H_2PtCl_6, $HAuCl_4$ or $PdCl_2$ as metal source in the presence of polyvinyl alcohol (PVA, MW = 10,000 g/mol; M/PVA mass ratio = 1.5:1). In a typical preparation, the M aqueous solution was first diluted 50 times with deionized water, and then an aqueous $NaBH_4$ solution (0.05 mol/L) with a M/$NaBH_4$ molar ratio of 1:5 was rapidly injected to the M sol and vigorously bubbled in ice–water bath for 20 min. Subsequently, a desired amount of the AgBr/3D-BiV support was added to the above mixture, and the obtained suspension was bubbled for 10 h to complete the deposition–adsorption process. Finally, the M/AgBr/3D-BiV sample was collected after filtration, drying at 200 °C for 2 h, washing with deionized water and alcohol, and further drying at 70 °C for 2 h. The Pd/3D-BiV sample was prepared according to the same procedure.

2.2. Photocatalyst characterization

All of the as-prepared samples were characterized using the inductively coupled plasma atomic emission spectroscopy (ICP-AES), X-ray diffraction (XRD), laser Raman spectroscopy, N_2 adsorption–desorption (BET), scanning electron microscopy (SEM), transmission electron microscopy (TEM), selected-area electron diffraction (SAED), Ultraviolet–visible (UV–vis) diffuse reflectance spectroscopy, and X-ray photoelectron spectroscopy (XPS). The detailed characterization procedures are described in the Supporting information.

2.3. Photocatalytic evaluation

The photocatalytic degradation of 4-CP with an initial concentration (C_0) of 15 mg/L over the as-prepared samples and the Degussa P25 (TiO_2) sample was conducted in a quartz reactor (QO250, Beijing Changtuo Sci. & Technol. Co., Ltd.) under visible-light irradiation, using a 400-nm cutoff filter and a 300-W Xe lamp (PLS-SXE300, Tianjin Dongli teaching instrument factory) [17]. The reactant solution was kept at RT through the flowing cool water and bubbled all the time. Prior to light illumination, the suspension (0.05 g of the sample in 100 mL of 4-CP solution in the presence of 0.6 mL of H_2O_2 aqueous solution (30 wt%)) was first ultrasonically treated for 0.5 h and then magnetically stirred in the dark for 1 h to reach the adsorption–desorption equilibrium of 4-CP on the photocatalyst surface. During the visible-light irradiation, 5 mL of the suspension was sampled at given time intervals and centrifuged to remove the photocatalyst. The absorption spectra of the degraded solutions were recorded on the aforementioned UV–vis spectrophotometer. The photocatalytic 4-CP degradation efficiency of each sample was calculated according to the absorbance intensity at 287 nm. Meanwhile, the product contents of degraded solutions under specific conditions were also measured using the electrospray ionization mass spectrometric (ESI-MS) technique.

3. Results and discussion

3.1. Crystal stucture and composition

Fig. 1 illustrates the XRD patterns of the samples. Apparently, all of the diffraction peaks could be well indexed to monoclinic $BiVO_4$ (JCPDS PDF# 75-1867). No diffraction signals assignable to the loaded AgBr or noble metal phases were recorded in the supported samples, indicating the uniform distribution of these species on the surface of 3DOM $BiVO_4$. The real loading of AgBr in the

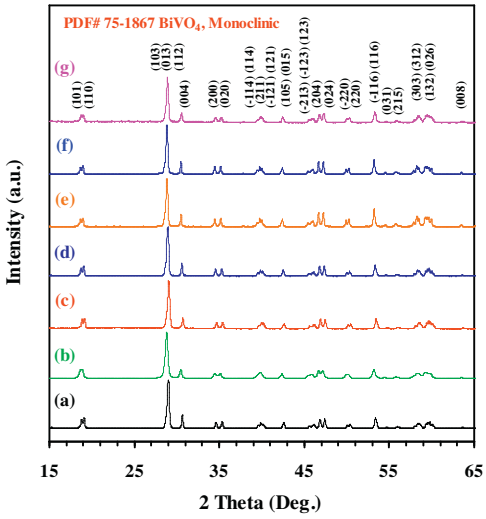

Fig. 1. XRD patterns of (a) BiV-bulk, (b) 3D-BiV, (c) AgBr/3D-BiV, (d) Pt/AgBr/3D-BiV, (e) Au/AgBr/3D-BiV, (f) Pd/AgBr/3D-BiV, and (g) Pd/3D-BiV.

AgBr/3D-BiV sample was 12.8 wt% (Table 1) according to the ICP-AES result; however, it decreased to 4.9, 3.5, and 3.4 wt% in the M/AgBr/3D-BiV (M=Pt, Au, and Pd) samples with the M loading of ca. 0.17 wt%, respectively. The grain sizes of all of the samples were in the range of 22–30 nm (Table 1). As shown in Fig. 2, the Raman bands at 126, 208, 324, 367, 638, 705, and 828 cm^{-1} were due to the V—O bonds in different vibrational modes of monoclinic $BiVO_4$ [19]. A small Raman band at 141 cm^{-1} was observed in the AgBr/3D-BiV sample, indicating the possible presence of a strong interaction between AgBr and V—O bond. The two absorption bands at 740 and 845 cm^{-1} in the FT-IR spectra of the samples were due to the asymmetrical and symmetrical stretching vibrations of VO_4^{3-} tetrahedron in $BiVO_4$ [20]. No signals attributable to the organics were recorded, suggesting that all of the organics were totally removed from the samples.

3.2. Morphology, pore structure, and surface area

Fig. 3 shows the SEM images of the 3D-BiV and BiV-bulk samples. The 3D-BiV sample displayed a periodically and hierarchically macroporous architecture, whereas the BiV-bulk sample was composed of micro/nano-sized particles. Fig. 4 shows the typical TEM images of the 3D-BiV-supported samples. Obviously, the 3DOM structure maintained quite well even after loading AgBr and/or M, and there were some mesopores on the nanoscale ligaments (20 ~ 30 nm in diameter) with tunable large pore volume (e.g., 0.112 cm^3/g for Pd/AgBr/3D-BiV). Interestingly, under the radiation of high-energy electron beam, the initially smooth ligaments started to get rough, accompanying by the in situ rapid growth and crystallization of some particles on the support (see the areas of 1–4 in Fig. 4). The recording of blurry diffraction rings (insets of Fig. 4d, i, m, r, and u) further suggests the formation of polycrystallites and the weak crystallinity of the 3DOM-structured samples. The lattice spacings (*d* value) were ca. 0.46 and 0.30 nm (Fig. 4d, e, i, m, r, and u), rather close to those of the (0 1 1) and (1 1 2) planes of monoclinic $BiVO_4$, respectively. It should be noted that no noble metal particles were clearly observed from the TEM images, implying the

Table 1
AgBr and noble metal (M) loadings, average crystallite sizes, BET surface areas, pore volumes, bandgap energies (E_g), and surface element compositions of the samples.

Sample	AgBr/M loading[a] (wt%)	D[b] (nm)	Surface area (m^2/g)/pore volume (cm^3/g)			E_g (eV)	Surface element composition (mol/mol)			
			>50 nm	<50 nm	Total		V/Bi	Ag/Bi	M/Bi	O_{ads}/O_{latt}
BiV-bulk	–/–	27.0	–	–	5.8	2.54	–	–	–	–
3D-BiV	–/–	22.3	1.9/0.035	24.6/0.033	26.5/0.068	2.56	1.32	–	–	2.60
AgBr/3D-BiV	12.8/–	26.1	5.4/0.084	9.3/0.027	14.7/0.111	2.61	2.18	0.140	–	0.19
Pt/AgBr/3D-BiV	4.9/0.166	29.2	4.7/0.080	13.4/0.029	18.1/0.109	2.55	1.14	0.069	0.10	0.47
Au/AgBr/3D-BiV	3.5/0.168	28.5	4.1/0.059	15.8/0.026	19.9/0.085	2.55	1.06	0.075	0.09	0.43
Pd/AgBr/3D-BiV	3.4/0.167	29.8	4.9/0.078	8.0/0.034	15.9/0.112	2.49	0.92	0.090	0.24	0.61
Pd/3D-BiV	–/0.165	25.2	4.0/0.057	13.5/0.021	17.5/0.078	2.52	–	–	–	–

[a] The data were obtained by the ICP-AES technique.
[b] The data were calculated according to the Scherrer equation using the FWHM of the (1 1 2) line of $BiVO_4$ in the XRD patterns.

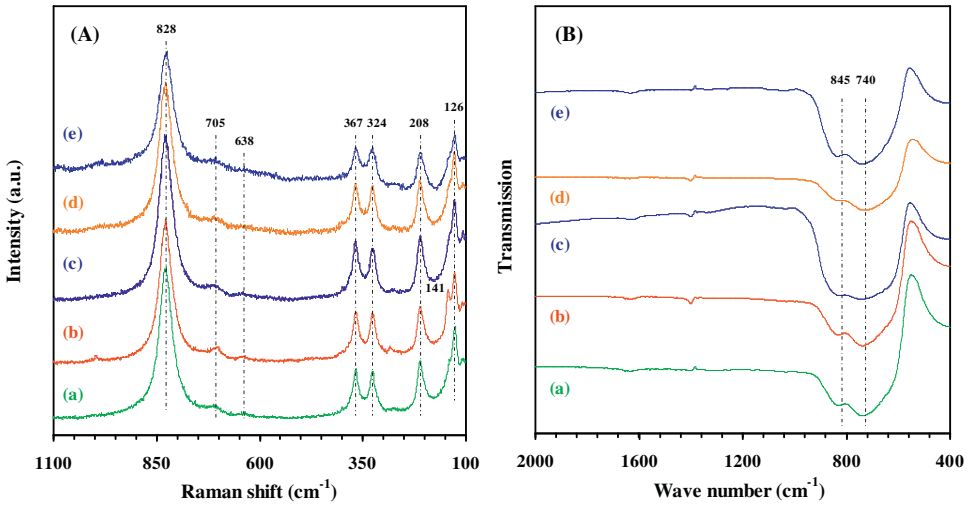

Fig. 2. Laser Raman spectra of (a) 3D-BiV, (b) AgBr/3D-BiV, (c) Pt/AgBr/3D-BiV, (d) Au/AgBr/3D-BiV, and (e) Pd/AgBr/3D-BiV.

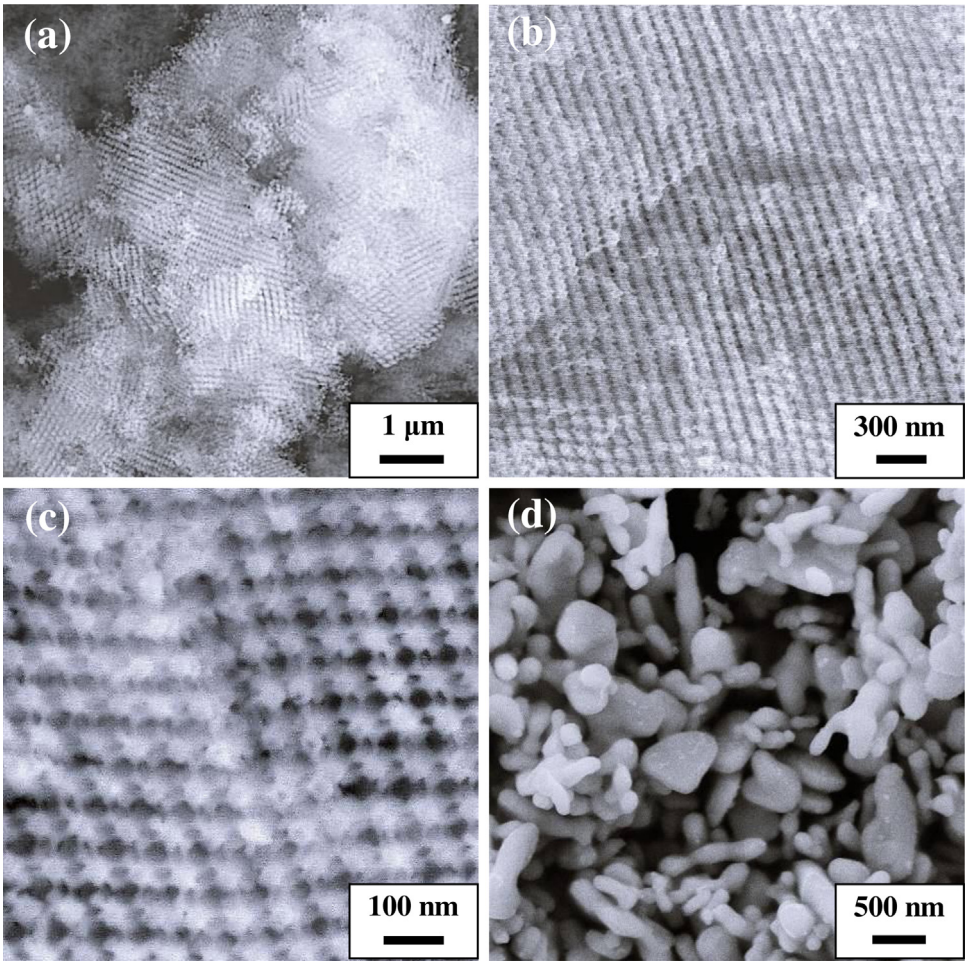

Fig. 3. SEM images of (a–c) 3D-BiV and (d) BiV-bulk.

possible formation of small nanoclusters on the low-crystallinity surface. The N_2 adsorption–desorption isotherms and pore-size distributions of the samples are illustrated in Fig. 5. The obvious macroporous structure enabled each of the samples to exhibit a type II isotherm with a type H3 hysteresis loop in the relative pressure range of 0.9–1.0 (Fig. 5A). As can be seen from Table 1, the loading of AgBr or M caused the surface area of the 3D-BiV sample to reduce (e.g., 26.5 m^2/g for 3D-BiV, 14.7 m^2/g for AgBr/3D-BiV, and 17.5 m^2/g for Pd/3D-BiV) and its pore volume (0.068 cm^3/g) to rise. The specific surface area (5.8 m^2/g) of the BiV-bulk sample was much lower than those (14.7–26.5 m^2/g) of the 3DOM-structured samples. Besides the obvious presence of macropores and mesopores in these samples, the $dV/d(\log D)$ values at decreased with the rise in pore size from 1.7 to 4.0 nm (Fig. 5B), indicating the possible presence of a small amount of micropores. Undoubtedly, the well-defined 3DOM structure with abundant nanopores and large surface areas is beneficial for capturing visible light and adsorbing small molecules on the active surface of these samples.

3.3. Optical behavior

Fig. 6 shows the light absorption properties of the samples. Compared to the 3D-BiV sample, the BiV-bulk sample exhibited a wider light absorption region in the range of 400–520 nm and weaker responsive intensity in the range of 520–800 nm, indicating the role of high crystallinity [21,22] and the stronger light absorption ability of the 3DOM structure. The loading of AgBr slightly decreased the visible-light absorption ascribed to the filtration of massive AgBr to the pores of 3D-BiV. Further loading a trace amount of M gave rise to the enhancement in visible-light absorption of the M/AgBr/3D-BiV samples as the load of AgBr decreased to a moderate amount. Otherwise, the bandgap energies (E_g) of these samples could be seen to increase in the order of Pd/AgBr/3D-BiV (2.49 eV) < BiV-bulk (2.52 eV) < Pd/3D-BiV (2.54 eV) < Pt or Au/AgBr/3D-BiV (2.55 eV) < 3D-BiV (2.56 eV) < AgBr/3D-BiV (2.61 eV).

3.4. Surface element composition, metal oxidation state, and oxygen adspecies

The surface compositions, chemical state, and oxygen adspecies of the samples were investigated by the XPS technique. Fig. 7 illustrates the Bi 4f, V $2p_{3/2}$, O 1s, Ag 3d, Pt 4f, Au 4f, and Pd 3d XPS spectra of the 3D-BiV, AgBr/3D-BiV, and M/AgBr/3D-BiV samples. The two signals at binding energy (BE) = 159.1 and 164.3 eV as well as the satellites at BE = 160.2–161.6 eV and 165.3–165.6 eV were ascribed to the surface Bi^{3+} ($4f_{7/2}$) and Bi^{3+} ($4f_{5/2}$) species [16], respectively. For the V $2p_{3/2}$ XPS spectra of the samples, all of the peaks could be assigned to the surface V species in the $BiVO_4$ phase. For the AgBr/3D-BiV samples modified by Pt and Pd, only V^{5+} species at BE = 516.7 eV could be observed, but additional signal due to the surface V^{4+} species at BE = 515.0–515.6 eV was also recorded on the AgBr/3D-BiV and Au/AgBr/3D-BiV samples, indicating that there were more oxygen vacancies on the surface of the latter two samples [16,17]. It is known that the generation of oxygen vacancies is beneficial for the activation of oxygen molecules on the samples, thus promoting the degradation of 4-CP. Obviously, a certain

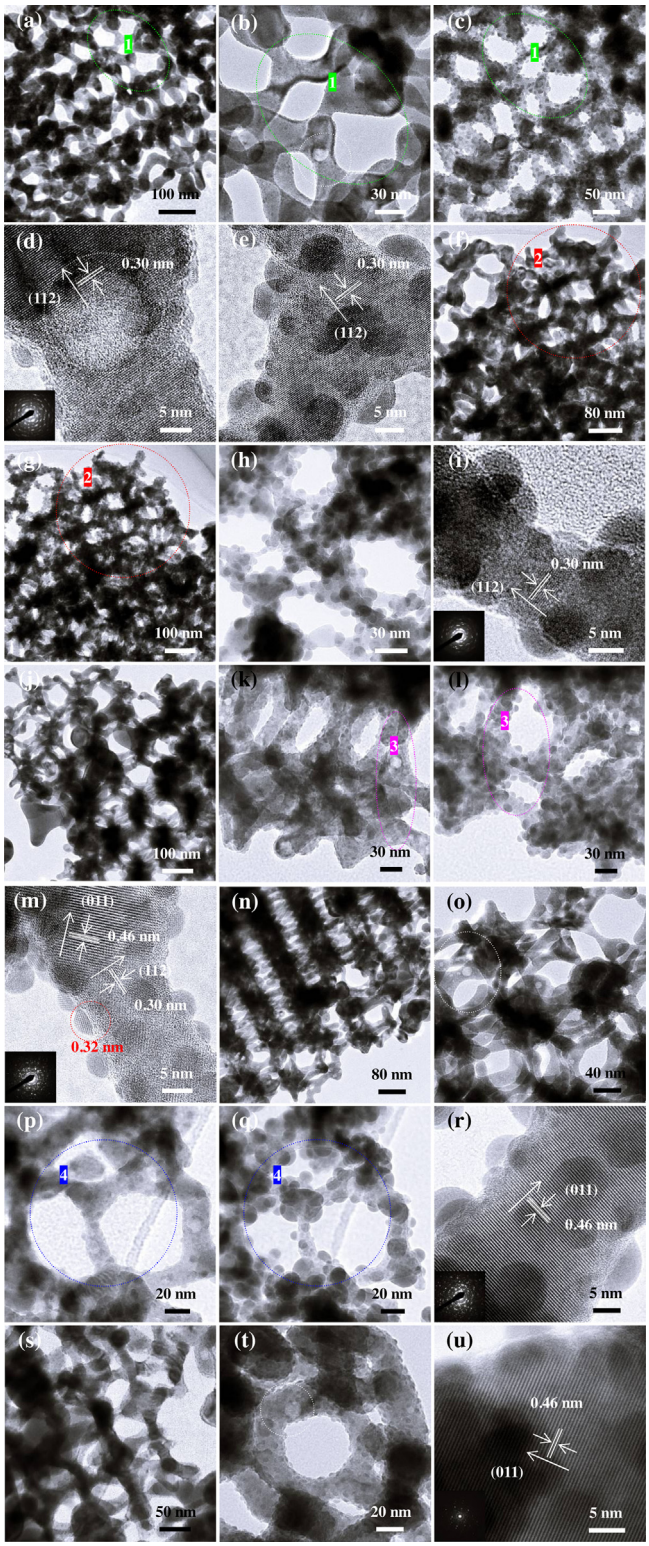

Fig. 4. TEM images and SAED patterns (insets) of (a–e) AgBr/3D-BiV, (f–i) Pt/AgBr/3D-BiV, (j–m) Au/AgBr/3D-BiV, (n–r) Pd/AgBr/3D-BiV, and (s–u) Pd/3D-BiV.

reconstruction took place on the surface electronic structure of AgBr/3D-BiV after it was modified by plasmonic noble metals, similar to that observed in the case of M/InVO$_4$-BiVO$_4$ [17]. From Fig. 7C, one can see two signals at BE = 531.8 and 529.7 eV, corresponding to the surface adsorption oxygen species (O_{ads}, e.g., O^-, O_2^{2-} or O_2^-) and lattice oxygen species (O_{latt}) [23]. The loading of only AgBr led to a significant reduction in surface O_{ads}/O_{latt} molar ratio and thus caused the AgBr/3D-BiV sample to possess the lowest surface O_{ads} concentration (Table 1), suggesting the shielding effect of excessive AgBr on the surface BiVO$_4$ (see the ICP-AES results). Thanks to the high oxygen-adsorption capacity of noble metals [24,25] as well as the loss of AgBr, the surface O_{ads} concentration much rebounded over each of the M/AgBr/3D-BiV samples, particularly the Pd/AgBr/3D-BiV sample with the highest M/Bi (0.24) and O_{ads}/O_{latt} (0.61) molar ratios. Generally speaking, for an oxygen-deficient catalyst, the higher the surface O_{ads} concentration, the larger amount of oxygen vacancies it possesses, and then the better is its activity [16]. The surface adsorbed oxygen species are the active oxygen species that could be converted to $^{\bullet}O_2^-$ free radicals, and the $^{\bullet}O_2^-$ free radicals then react with 4-CP to generate CO_2 and H_2O, hence enhancing the photocatalytic activities of the samples. The deviation in BE of the surface Ag species on the AgBr/3D-BiV and M/AgBr/3D-BiV samples (Fig. 7D) implies the interaction present between M nanoclusters and AgBr. However, one could not exclude the presence of metallic Ag due to the similar BEs of Ag^0 and Ag^+ species [26]. According to the Pt 4f, Au 4f, and Pd 3d XPS spectra in the insets of Fig. 7D, there were Pt^0, Au^0, Pd^0, and Pd^{2+} species present on the surface of the various samples, respectively. It is worth noting that the surface V concentration on the AgBr/3D-BiV sample (V/Bi = 2.18) was much higher than that on the 3D-BiV sample (V/Bi = 1.32), and its surface enrichment degree decreased significantly after the loading of noble metals, further reflecting the restructuring phenomenon mentioned above.

3.5. Photocatalytic performance

Fig. 8 and Fig. S1 show the photocatalytic activities of the samples for the degradation of 4-CP (15 mg/L) with the assistance of H_2O_2 (0.6 mL) under visible-light irradiation, in which $^{\bullet}O_2^-$ and $^{\bullet}OH$ free radicals are usually considered to be the active species [4,7,8]. It is apparent that the commercial TiO$_2$ (Fig. S1(A)) exhibited poor photocatalytic activity for the degradation of 4-CP within 180 min. The performance of the bulk BiVO$_4$ sample (Fig. S1(B)) with high crystallinity was much better due to its sensitivity to visible light, but its degradation effect was still not so good in the given irradiation time. Moreover, the two small adsorption peaks centered at 335 and 435 nm in the absorbance spectrum of TiO$_2$ were not observed from the absorbance spectrum of bulk BiVO$_4$, which might be associated with formation of some intermediates. The results indicate the possible presence of different degradation pathways of 4-CP in the two cases. As expected, with the great help of a small amount of H_2O_2 in the initial reaction solution (Fig. S1(C and D)), the 4-CP degradation became more effective over the 3D-BiV sample under visible-light irradiation, demonstrating the superiority of the 3DOM nanostructure with a developed pore structure and a large surface area that could enhance the photocatalytic performance. Furthermore, by comparing the photocatalytic activities of the typical samples (e.g., bulk-BiV < 3D-BiV < Pd/3D-BiV < Pd/AgBr/3D-BiV) as well as their absorbance spectra, one can clearly see the significant influences induced by the plasmonic effect of Pd nanoclusters, heterojunctions generated by loading of an appropriate amount of AgBr, and synergistic effects between Pd or AgBr ($Ag^+ \leftrightarrow Ag^0$) and BiVO$_4$. The AgBr/3D-BiV sample modified by 10 wt% AgBr exhibited a reduced performance (Fig. S1(E)), which might be caused by the shielding effect of excessive AgBr in visible-light spectrum on the 3DOM BiVO$_4$ support. A similar light intensity influence could also be observed by monitoring the 4-CP degradation over the Au/AgBr/3D-BiV sample, in which the degradation rate started to become slow as soon as light intensity was weakened after irradiation for 40 min (Fig. S1(F)). Although the Pt/AgBr/3D-BiV sample (Fig. S1(G)) showed shoulder peaks at 335 and 445 nm similar to those of the

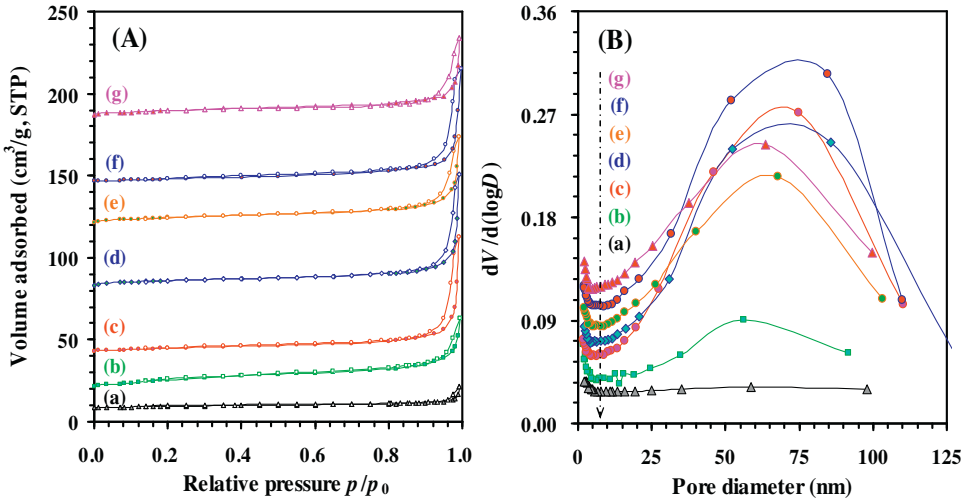

Fig. 5. (A) N_2 adsorption–desorption isotherms and (B) pore-size distributions of (a) BiV-bulk, (b) 3D-BiV, (c) AgBr/3D-BiV, (d) Pt/AgBr/3D-BiV, (e) Au/AgBr/3D-BiV, (f) Pd/AgBr/3D-BiV, and (g) Pd/3D-BiV.

AgBr-modified samples and a better activity than the AgBr/3D-BiV sample, it was inferior to both of the Pd-modified samples (Fig. 8B and Fig. S1(H)) in the removal of 4-CP under visible-light irradiation. This result suggests the distinct plasmonic effects of different noble metals. Obviously, due to the formation of heterostructures that could accelerate the separation and transfer of the photogenerated carries, the Pd/AgBr/3D-BiV sample showed much better photocatalytic performance than the Pd/3D-BiV sample. Meanwhile, this well-developed photocatalyst also outperformed the other as-reported materials for the photocatalytic removal of 4-CP under visible-light irradiation, such as $ZnFe_2O_4$ nanotube [2], $ZnFe_2O_4$/RGO [4], $Bi_xTi_{1-x}O_2$ with core–shell structure [6], and Ag–AgI/Fe_3O_4@SiO_2 [8], and so on (Table S1 of the Supplementary material). Since AgX (X=Cl, Br, and I) photocatalysts possess quite similar properties (e.g., light absorption capacity, energy band structure or semiconductor type), if there was a trace amount of Cl^- ions in the main phase of the AgBr-based photocatalysts, it would not have a significant impact on the photocatalytic performance of the samples [8].

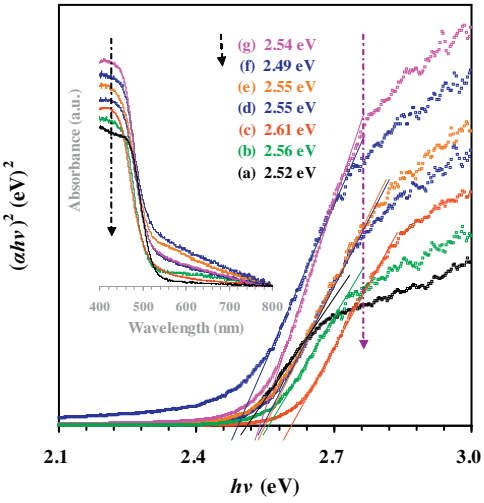

Fig. 6. Plots of $(\alpha h\upsilon)^2$ versus $h\upsilon$ and UV–vis diffuse reflectance spectra (inset) of (a) BiV-bulk, (b) 3D-BiV, (c) AgBr/3D-BiV, (d) Pt/AgBr/3D-BiV, (e) Au/AgBr/3D-BiV, (f) Pd/AgBr/3D-BiV, and (g) Pd/3D-BiV.

Up to date, several degradation routes of 4-CP in the Fenton-type reaction under visible-light irradiation have been proposed in the literature. For instance [1]:

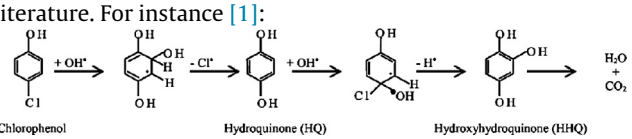

In this study, we also tried to make clear the specific degradation process of 4-CP over our samples through analyzing some typical reaction solutions at different reaction time by the ESI-MS technique. At the beginning of light irradiation (Fig. 8B and C and S1(I)), there was co-presence of organic fragments with m/z of 97 (close to the molecular weight of 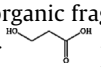), 101 (i.e., 97 + 4), 117 (i.e., 101 + 16, close to the molecular weight of 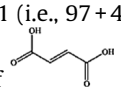), 121 (i.e., 117 + 4), 127, 131 (i.e., 127 + 4), 143 (i.e., 127 + 16, close to the molecular weight of 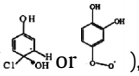 or), and 147 (i.e., 143 + 4), indicating that there were several kinds of intermediates in the solutions after the pretreatment in the dark [2,27]. It is apparent that the highest absolute intensity stayed basically at the m/z range of 127–131 in the whole degradation process, which possibly corresponded to the initial 4-CP and as-generated HHQ during the reaction. The fragment with m/z = 126.8 (Fig. 8C) showed a much higher intensity over the 3D-BiV sample in the presence of H_2O_2 than those over the other samples in the absence of H_2O_2, implying that H_2O_2 (or •OH free radicals) also played an important role in the initial degradation of 4-CP in the dark (i.e., 4-CP → ... → HHQ). No remarkable fragments were detected in the reaction solution of the Pd/AgBr/3D-BiV sample after 150 min (Fig. 8B), suggesting the complete removal of the organic molecules. Obviously, these results agree well with those observed in the absorbance spectra of the reaction solutions, including the existence and extinction of the adsorption bands at 335 and 445 nm. Similarly, the ESI-MS result together with the absorbance spectra confirm its relative low activity of the AgBr/3D-BiV sample for 4-CP degradation. By considering the evolutions of main fragments with m/z = 127–131 and the above two adsorption bands of Pd/AgBr/3D-BiV and AgBr/3D-BiV, one can realize that the former showed much better performance than the latter. That is to say, the loading of Pd nanoclusters was favorable for the conversion of 4-CP to some intermediates in the dark, which be then oxidized into small molecules easily under irradiation. The red or blue shift of

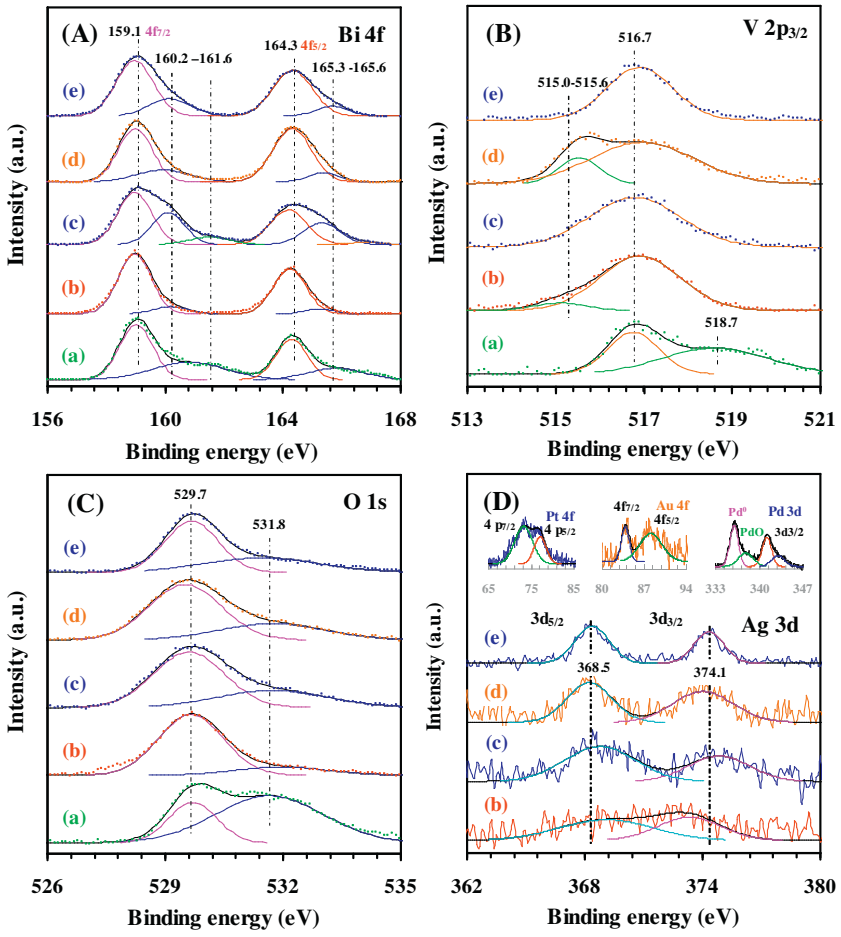

Fig. 7. (A) Bi 4f, (B) V $2p_{3/2}$, (C) O 1s, and (D) Ag 3d as well as Pt 4f, Au 4f, and Pd 3d (insets) XPS spectra of (a) 3D-BiV, (b) AgBr/3D-BiV, (c) Pt/AgBr/3D-BiV, (d) Au/AgBr/3D-BiV, and (e) Pd/AgBr/3D-BiV.

the specific adsorption wavelength at maximal intensity (Fig. S1(J)) could further reflect the general degradation process of 4-CP. Due to formation of some intermediates, the changing trend in wavelength varied from the various samples, signifying the possible occurrence of different 4-CP degradation routes over the samples. Furthermore, the basically unchanged TEM images and SAED pattern of the AgBr/3D-BiV sample after 3 h of 4-CP degradation (Fig. 9) indicate that this photocatalyst exhibited high photocatalytic stability.

From the above results and discussion, one can realize that the excellent photocatalytic performance of Pd/AgBr/3D-BiV for 4-CP degradation could be ascribed to the high-efficiency light harvesting and the effective transfer and separation of photogenerated carriers through the 3DOM nanoarchitecture. It was also easy for the organics to diffuse through the high-porosity structure and adsorb on the porous surface to react with active species. Furthermore, a moderate loading of AgBr with high visible-light stability could not only bring about abundant heterojunctions between AgBr and 3DOM $BiVO_4$ that exhibited a high visible-light response and greatly facilitate the effective utilization of the carriers, but also generate synergistic effects between Ag ($Ag^+ \leftrightarrow Ag$) species

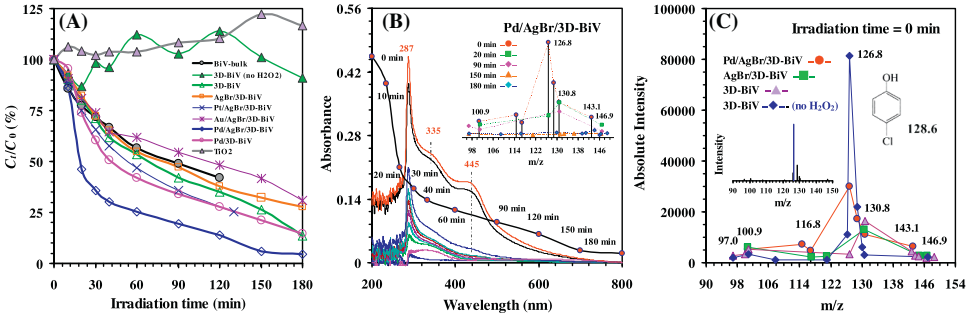

Fig. 8. (A) Degradation efficiency versus reaction time over the as-prepared and commercial TiO_2 samples for the degradation of 4-CP (C_0 = 15 mg/L) aqueous solution under visible-light (λ > 400 nm) irradiation, (B) absorbance versus reaction time as well as absolute intensity versus *m/z* (inset) of the Pd/AgBr/3D-BiV sample for the degradation of 4-CP (C_0 = 15 mg/L) aqueous solution under visible-light irradiation, and (C) absolute intensity versus *m/z* of the Pd/AgBr/3D-BiV, AgBr/3D-BiV, and 3D-BiV samples at the beginning of visible-light irradiation.

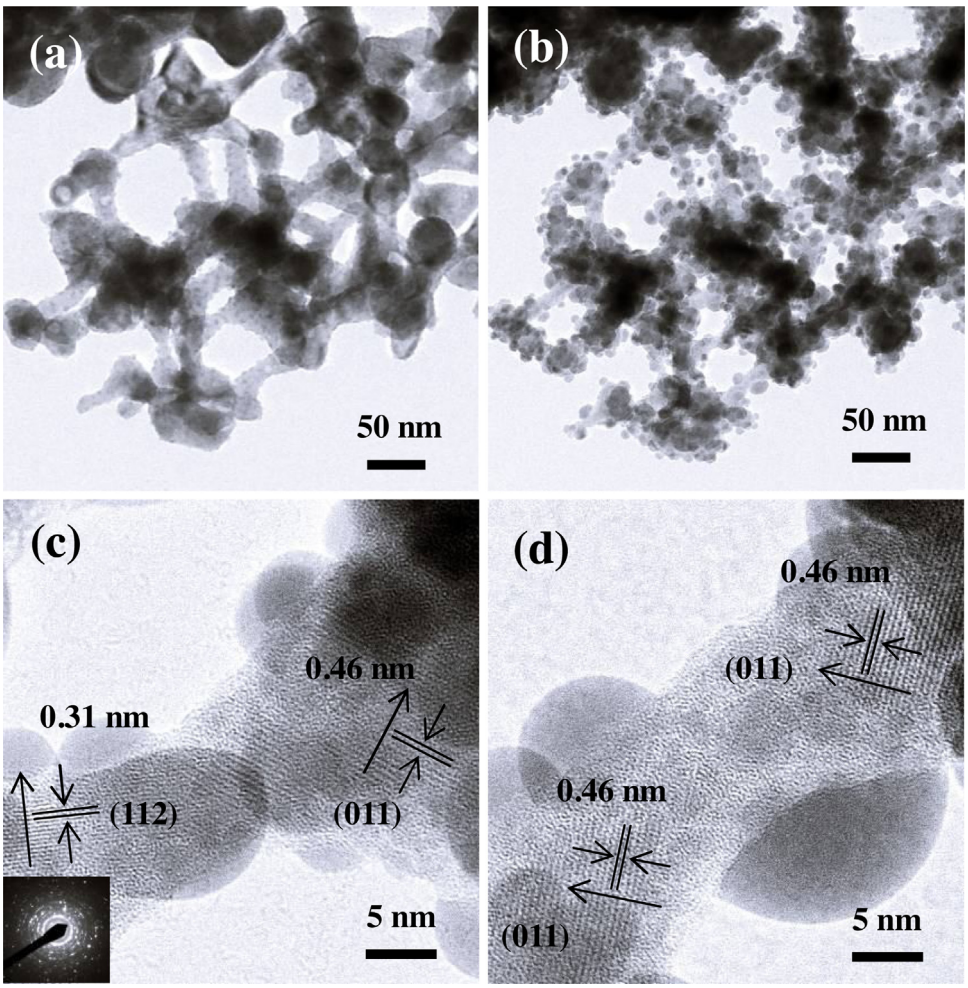

Fig. 9. TEM images and SAED pattern (inset) of the AgBr/3D-BiV sample after 3 h of 4-CP degradation (C_0 = 15 mg/L) under visible-light irradiation.

and Pd nanoclusters to strengthen the intrinsic plasmonic effect. In addition, the Pd nanoclusters could reduce the recombination probability of the carriers, and enhance the activation of oxygen molecules to the active oxygen species that would then react with the pollutant molecules to CO_2 and H_2O. Therefore, we believe that the well-developed tri-component Pd/AgBr/3D-BiV photocatalyst is a promising photocatalytic material for the removal of organic pollutants.

4. Conclusions

3DOM-structured $BiVO_4$ (3D-BiV), AgBr/3D-BiV, and 0.17 wt% M/AgBr/3D-BiV (M=Au, Pt, and Pd) could be fabricated via the PMMA-templating, low-temperature deposition, and PVA-protected reduction routes, respectively. All of these samples possessed a good-quality 3DOM structure and high surface areas. The AgBr and noble metals were highly dispersed on the surface of 3D-BiV. Among the M/AgBr/3D-BiV samples, 0.17 wt% Pd/AgBr/3D-BiV photocatalytically performed the best for the degradation of 4-CP under visible-light irradiation: Almost complete degradation of 4-CP was achieved within 150 min. We believe that the good 3DOM structure, high surface oxygen adspecies concentration, easy transfer and separation of photogenerated carriers, and synergistic effect between AgBr or Pd nanoclusters and $BiVO_4$ were responsible for the excellent photocatalytic performance of 0.17 wt% Pd/AgBr/3D-BiV.

Acknowledgements

This work was supported by the NSF of China (21377008), 2013 Education and Teaching – Postgraduate Students Education – 2011 Beijing Municipality Excellent Ph.D. Thesis Supervisor (20111000501), 2013 Education and Teaching – Postgraduate Students Cultivation – National Excellent Ph.D. Thesis Supervisor and Cultivation Base Construction (005000542513551), the Foundation on the Creative Research Team Construction Promotion Project of Beijing Municipal Institutions, Scientific Research Base Construction – Science and Technology Creation Platform – National Materials Research Base Construction, and Doctoral Innovation Fund of Beijing University of Technology (YB201310).

Appendix A. Supplementary data

Supplementary data associated with this article can be found, in the online version, at http://dx.doi.org/10.1016/j.apcatb.2014.12.045.

References

[1] P. Wongwisate, S. Chavadej, E. Gulari, T. Sreethawong, P. Rangsunvigit, Desalination 272 (2011) 154–163.
[2] X.Y. Li, Y. Hou, Q.D. Zhao, W. Teng, X.J. Hu, G.H. Chen, Chemosphere 82 (2011) 581–586.
[3] Y. Hou, X.Y. Li, Q.D. Zhao, G.H. Chen, C.L. Raston, Environ. Sci. Technol. 46 (2012) 4042–4050.

[4] Y. Hou, X.Y. Li, Q.D. Zhao, G.H. Chen, Appl. Catal. B 142–143 (2013) 80–88.
[5] Y.M. Lin, D.Z. Li, J.H. Hu, G.C. Xiao, J.X. Wang, W.J. Li, X.Z. Fu, J. Phys. Chem. C 116 (2012) 5764–5772.
[6] Z.F. Bian, J. Ren, J. Zhu, S.H. Wang, Y.F. Lu, H.X. Li, Appl. Catal. B 89 (2009) 577–582.
[7] L.J. Xu, J.L. Wang, Environ. Sci. Technol. 46 (2012) 10145–10153.
[8] J.F. Guo, B.W. Ma, A.Y. Yin, K.N. Fan, W.L. Dai, Appl. Catal. B 101 (2011) 580–586.
[9] N.C. Castillo, L. Ding, A. Heel, T. Graule, C. Pulgarin, J. Photochem. Photobiol. A 216 (2010) 221–227.
[10] J. Yin, Z.G. Zou, J.H. Ye, Chem. Phys. Lett. 378 (2003) 24–28.
[11] B. Neppolian, L. Ciceri, C.L. Bianchi, F. Grieser, M. Ashokkumar, Ultrason. Sonochem. 18 (2011) 135–139.
[12] H. Tada, T. Mitsui, T. Kiyonaga, T. Akita, K. Tanaka, Nat. Mater. 5 (2006) 782–786.
[13] L.S. Zhang, K.H. Wong, Z.G. Chen, J.C. Yu, J.C. Zhao, C. Hu, C.Y. Chan, P.K. Wong, Appl. Catal. A 363 (2009) 221–229.
[14] Y. Hou, X.Y. Li, Q.D. Zhao, X. Quan, G.H. Chen, J. Mater. Chem. 21 (2011) 18067–18076.
[15] L. Suljo, C. Phillip, B.I. David, Nat. Mater. 10 (2011) 911–921.
[16] Y.X. Liu, H.X. Dai, J.G. Deng, L. Zhang, C.T. Au, Nanoscale 4 (2012) 2317–2325.
[17] K.M. Ji, J.G. Deng, H.J. Zang, J.H. Han, H. Arandiyan, H.X. Dai, Appl. Catal. B 165 (2015) 285–295.
[18] X. Meng, L. Zhang, H.X. Dai, Z.X. Zhao, R.Z. Zhang, Y.X. Liu, Mater. Chem. Phys. 125 (2011) 59–65.
[19] H.Y. Jiang, H.X. Dai, X. Meng, K.M. Ji, L. Zhang, J.G. Deng, Appl. Catal. B 105 (2011) 326–334.
[20] R.L. Frost, D.A. Henry, M.L. Weier, W. Martens, J. Raman Spectrosc. 37 (2006) 722–732.
[21] S.W. Liu, L.S. Zhang, H.L. Xu, W. Zhu, L. Zhou, W.Z. Wang, J. Mol. Catal. A 252 (2006) 120–124.
[22] J.Q. Yu, Y. Zhang, A. Kudo, J. Solid State Chem. 182 (2009) 223–228.
[23] K.M. Ji, H.X. Dai, J.G. Deng, L.Y. Song, B.Z. Gao, Y. Wang, X.W. Li, Appl. Catal. B 129 (2013) 539–548.
[24] Y.C. Wei, J. Liu, Z. Zhao, Y.S. Chen, C.M. Xu, A.J. Duan, G.Y. Jiang, H. He, Angew. Chem. Int. Ed. 50 (2011) 2326–2329.
[25] C.R. Chang, X.F. Yang, B. Long, J. Li, ACS Catal. 3 (2013) 1693–1699.
[26] T.T. Li, Y.M. He, H.J. Lin, J. Cai, L.Z. Dong, X.X. Wang, M.F. Luo, L.H. Zhao, X.D. Yi, W.Z. Weng, Appl. Catal. B 138–139 (2013) 95–103.
[27] E. Grabowska, J. Reszczyńska, A. Zaleska, Water Res. 46 (2012) 5453–5471.